

BayesTME: A reference-free Bayesian method that discovers spatial transcriptional programs in the tissue microenvironment

Haoran Zhang¹, Miranda V. Hunter², Mingyuan Zhou³, Richard White², Wesley Tansey^{4*}

¹Department of Computer Science, University of Texas at Austin

²Sloan Kettering Institute

³McCombs School of Business, University of Texas at Austin

⁴Department of Epidemiology and Biostatistics, Memorial Sloan Kettering Cancer Center

Abstract

Spatial variation in cellular phenotypes underlies immune recognition and response to therapy in many diseases. Spatial transcriptomics holds the potential to quantify such variation, but existing analysis methods require reference single-cell RNA-seq (scRNA-seq) data to model phenotypes and therefore often miss phenotypes present only in the spatial transcriptomics data. We present BayesTME, a reference-free Bayesian method that detects phenotypes directly from spatial transcriptomics data. BayesTME outperforms both scRNA-seq integrated and reference-free methods in tasks including bleed correction, cell type detection, spot deconvolution, and cellular community segmentation. Further, BayesTME models each phenotype as spatially adaptive and discovers statistically significant spatial patterns amongst coordinated subsets of genes within phenotypes, which we term spatial transcriptional programs. On real tissues from human and zebrafish melanoma, BayesTME identifies spatial transcriptional programs that capture core biological concepts like bilateral symmetry, differential expression between interior and surface tumor cells, and tumor-associated fibroblast and macrophage reprogramming. Our results demonstrate BayesTME’s power in analyzing spatial transcriptomics data and fostering a deeper understanding of the spatial architecture of the tissue microenvironment.

1 Introduction

The tissue microenvironment (TME) is composed of a heterogeneous mixture of cell phenotypes, subtypes, and spatial structure. The composition of the TME impacts disease progression and therapeutic response. For instance, the composition of immune cells in the tumor microenvironment is a determinant of response to immunotherapy (IO) (Kalbasi and Ribas, 2020). More recent work suggests that it is not cellular composition but rather the *spatial organization* of the microenvironment that determines IO response (Herbst et al., 2014; Gajewski et al., 2013; Spranger et al., 2013; Echarti et al., 2019). Spatially-unaware approaches, such as single-cell RNA and DNA sequencing (scRNA-seq and scDNA-seq), are able to capture the presence and abundance of different cell types and phenotypes (hereon referred to as simply types) (Navin et al., 2011), but are unable to characterize their spatial organization. Spatial measurements and spatial modeling of the tissue microenvironment *in situ* present an opportunity to fully uncover and understand the role that spatial structure plays in determining disease progression and therapeutic response.

Spatial transcriptomics (ST) technologies, such as Visium (10x Genomics, 2022), HDST (Vickovic et al., 2019), and Slide-seq (Rodrigues et al., 2019) enable biologists to measure spatially-resolved gene expression levels at thousands of spots in an individual tissue. Each tissue is divided into a grid or lattice of spots, with each spot in the grid typically 50–100 μm wide. The tissue is permeabilized to release mRNAs to capturing

*Corresponding email: tanseyw@mskcc.org

probes with spot-specific barcodes. Bulk RNA-seq is then run on the captured mRNAs with spatial barcode tags. The result is a high-dimensional, spatially-localized gene expression count vector for a small number of cells per location.

Modeling spot-wise aggregate measurements is challenging as it requires disentangling four sources of spatial variation present in the raw signal. (i) Technical error, also known as spot bleeding, causes mRNAs to bleed to remote spots and contaminates the raw spatial signal. (ii) Variation in cell counts changes the absolute number of UMIs per spot. UMI counts scale with the number of cells in each spot. Conventional pre-processing methods like log-normalization break this linear relationship, requiring working with count data directly to accurately model cell counts. (iii) Differences in the proportions of cell types in each spot conflate signal strength with cell type prevalence. This complicates analysis as it necessitates performing a difficult deconvolution of each spot into its constituent cell type proportions. (iv) Finally, spatial variation of gene expression levels within cell types in response to the microenvironment affects the signal but is obscured by the first three sources of spatial variation. Teasing out these different sources of spatial variation in ST data is necessary to obtain a full understanding of the spatial architecture of the tissue microenvironment.

Several methods have been developed that specialize on a subset of these four sources of spatial variation. SpotClean (Ni et al., 2021) corrects spot bleeding by fitting an isotropic Gaussian model to raw UMI counts in order to map them back to their most likely original location. Spatial clustering methods (Zhao et al., 2021; Pham et al., 2020; Dries et al., 2021) fuse spots together to effectively capture regions of constant cell type proportion with varying cell counts. Spot deconvolution methods (Miller et al., 2021; Lopez et al., 2022; Kleshchevnikov et al., 2022) separate the aggregate signals into independent component signals with each attributable to a different cell type. Spatial differential expression methods (Sun et al., 2020; Svensson et al., 2018) assess the aggregate spot signal to detect regions where individual genes or gene sets follow a spatial pattern. While each of these methods has moved the field of ST analysis forward, they each have shortcomings such as making incorrect parametric assumptions, requiring reference scRNA-seq data, or only capturing aggregate signals rather than phenotype-specific ones.

Notably, most existing methods either do not perform spot deconvolution or assume cells of a given type have a stationary pattern of gene expression. This stationarity assumption is at conflict with the biological knowledge that cells change their behavior in response to the microenvironment under mechanisms including proliferation, invasion, and drug resistance (Quail and Joyce, 2013). The microenvironment regulates cell behavior and therefore alters gene expression profiles of specific cell phenotypes (Kim et al., 2017). These microenvironmental influences are particularly relevant in disease contexts. As an example, the microenvironment affects each phase of cancer progression and invasion-metastasis cascade (Ungefroren et al., 2011). Chronic inflammation is able to induce tumor initiation, malignant conversion, and invasion (Grivennikov et al., 2010). Recent research also shows cancer cells in the interior of a tumor behave differently than cancer cells at the interface with healthy cells (Hunter et al., 2021). Modeling ST data to understand the spatial structure of transcriptomic diversity in each cell type remains an important open problem.

Recently, reference-based methods have been proposed (Cable et al., 2021; Lopez et al., 2022) to capture this within-phenotype spatial variation. However, reference-based methods often fail to identify all cell types in ST data, resorting instead to specification of “unknown” cell types for phenotypes not found in the reference data. Further, these methods require post-hoc interpretation of spatial variation rather than a principled approach based on model uncertainty quantification. To-date, no methods fully meet the challenge of ST data: accurately deconvolving spots and capturing the within-phenotype spatial gene expression, without reference scRNA, while providing principled control of the statistical error rate.

In this paper, we present BayesTME, a reference-free Bayesian method that models all four sources of spatial variation in ST data. Figure 1 overviews the full BayesTME workflow and outputs. BayesTME uses a multiscale model of ST data with different spatial priors at each scale. It places spatial fusion priors between spots, adaptively fusing tissue regions together to reveal cellular community structure. At the same time, BayesTME places graph smoothing priors on within-phenotype gene expression. These priors enable BayesTME to discover spatial transcriptional programs (STPs), coordinated spatial gene expression patterns among groups of genes within a phenotype.

BayesTME also models the global pattern of spatial technical error present in raw ST data. As we

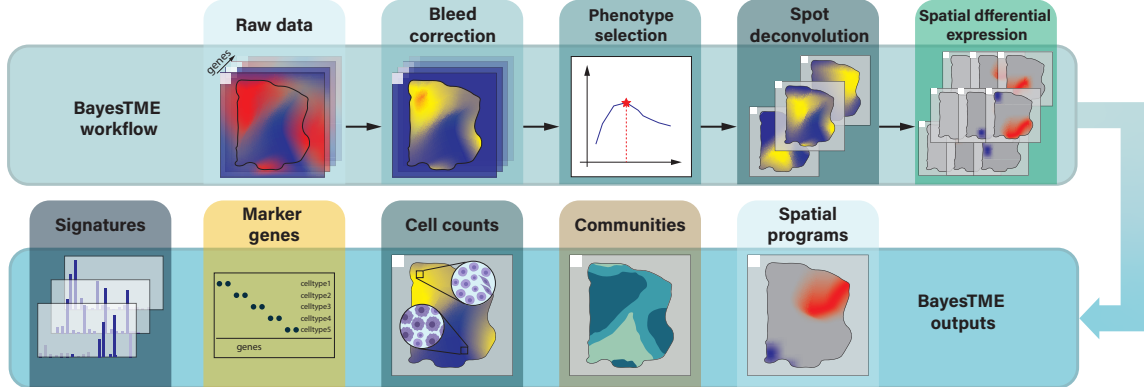


Figure 1: The BayesTME workflow and outputs. **Top:** BayesTME first corrects technical errors (spot bleeding) in the raw ST data by probabilistically mapping reads to their most likely original location in the tissue. An unbiased spatial cross-validation routine is then run to select the optimal number of unique cell phenotypes. The cell phenotype count is then fixed and a reference-free spot deconvolution is run to simultaneously recover cell phenotypes and their counts at each spot. Finally, the deconvolution model is augmented with a spatially-adaptive phenotype model to infer phenotype-specific spatial variations. **Bottom:** The final output of the complete BayesTME pipeline is the inferred cell phenotype expression signatures, the top marker genes that are maximally differentially expressed between phenotypes, the posterior distribution over the discrete cell counts of each type in each spot, the segmented tissue partitioned into cellular communities, and the spatial transcriptional programs discovered for each phenotype.

demonstrate, ST data contain technical error that is anisotropic: UMIs bleed toward a specific direction in each sample. We show how this directional bleeding leads existing isotropic preprocessing methods (Ni et al., 2021) to biased results. At the same time, ignoring such technical error leads methods to hallucinate spatial trends in gene expression that may not exist.

On benchmarks for bleed correction, cell type identification, spot deconvolution, and cellular community segmentation, BayesTME outperforms existing methods. Benchmarks for spatial gene expression detection illustrate the inability of aggregate spatial differentiation techniques to detect within-phenotype variation. Conversely, BayesTME identifies STPs with high power while maintaining tight control over the false discovery rate on the reported spatially-varying genes in each cell type. On real tissues from human melanoma and a zebrafish melanoma model, BayesTME identifies STPs that capture core biological concepts like bilateral symmetry and differential expression between the surface and interior tumor cells. BayesTME is open source¹, does not require reference scRNA-seq, and all hyperparameters are auto-tuned without the need for any manual user input.

2 Results

ST is all you need: Semi-synthetic benchmarks demonstrate BayesTME outperforms a suite of existing methods without needing scRNA reference data. We benchmarked BayesTME against other methods: BayesSpace (Zhao et al., 2021), cell2location (Kleshchevnikov et al., 2022), DestVI (Lopez et al., 2022), STdeconvolve (Miller et al., 2021), stLearn (Pham et al., 2020), and Giotto (Dries et al., 2021) on simulated data based on real single-cell RNA sequencing (scRNA) data. We randomly sampled K^* cell types from a previously-clustered scRNA dataset (Kleshchevnikov et al., 2022); we conducted experiments for K^* from 3 to 8. For a given K^* , we constructed spatial layouts consisting of 25 cellular communities, defined as spatially-contiguous regions of homogeneous mixtures of cell types. We randomly generated the total cell number for each spot with cellular-community-specific priors. After dividing the total cell number into K^*

¹<https://github.com/hurazh/bayestme>

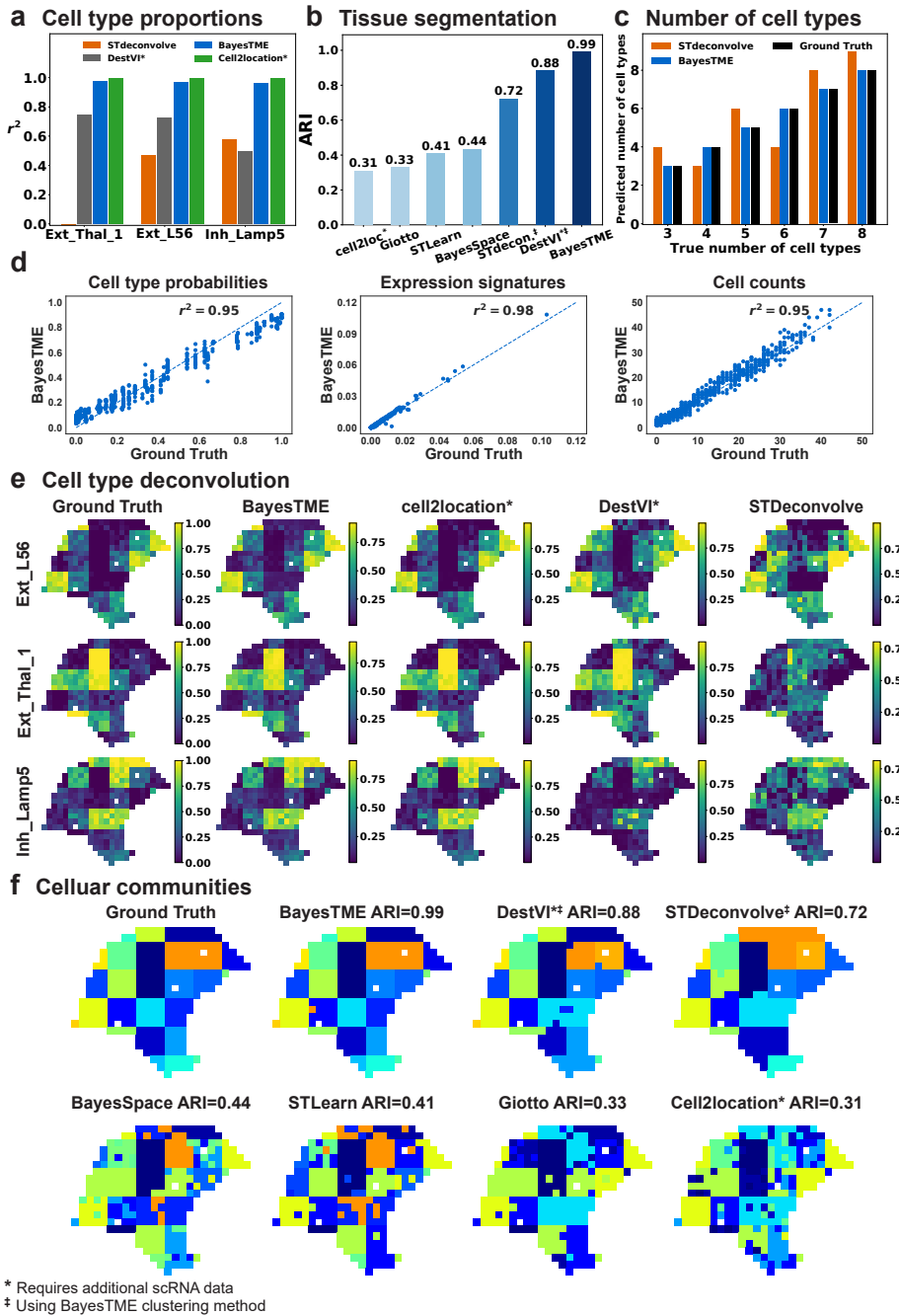


Figure 2: BayesTME performs favorably to existing methods in semi-synthetic benchmarks. (a.) Correlation of deconvolved cell type proportions in the $K^* = 3$ cell type benchmark. BayesTME (Pearson's $r = 0.97$) performs comparably to the best method cell2location (Pearson's $r = 0.99$, difference not significant); however, cell2location requires the ground truth scRNA reference whereas BayesTME is reference-free. (b.) BayesTME outperforms all other methods when segmenting the tissue into cellular communities, measured by adjusted Rand index (ARI). (c.) BayesTME is able to recover the correct number of cell types in each simulation by using an unbiased spatial cross-validation routine. (d.) BayesTME accurately recovers the ground truth cell type distributions, discrete cell counts, and expression signatures of each cell type in the simulation. (e.) Visualization of the deconvolution of the benchmarked methods. (f.) Visualization of the tissue segmentation results for the different methods.

cell types, we randomly sampled cells from the scRNA data of the selected cell types and mapped them on top of the spot pattern from a human melanoma tissue sample (Thrane et al., 2018); see the Supplement for details. We compared the performance of BayesTME to the above existing methods on selecting the correct number of cell phenotypes, deconvolving spots, segmenting tissues into spatial communities, and detecting groups of spatially-varying genes within phenotypes. As we demonstrate, BayesTME outperformed existing methods across all benchmark tasks.

BayesTME identifies cell types and determines cell type abundance. The core modeling task in ST analysis is deconvolution of the spots into their constituent cell phenotype proportions. BayesTME implements a novel discrete deconvolution algorithm and infers a posterior distribution over the discrete number of cells in each spot. We benchmarked BayesTME’s deconvolution by Pearson’s correlation (r) with the ground truth for cell type proportion against existing methods that provide proportional deconvolution. BayesTME recovered the cell type proportion with high accuracy (Pearson’s $r = 0.97$), outperforming the reference-free alternative STdeconvolve (Pearson’s $r = 0.34$) and scRNA-integrated DestVI (Pearson’s $r = 0.66$), and was comparable to cell2location (Pearson’s $r = 0.99$) which also requires scRNA reference (Figure 2a,e). BayesTME also provided an accurate estimation of the discrete number of cells of each type in each spot (Pearson’s $r = 0.95$, Figure 2d).

After deconvolution, BayesTME enables the user to segment the tissue into tissue segments representing cellular communities. In community detection benchmarks, BayesTME (adjusted Rand index (Hubert and Arabie, 1985), $ARI = 0.99$) surpassed all other currently available alternatives (Figure 2 b,f), including both spatial clustering (BayesSpace, STLearn, Giotto) and spot deconvolution (cell2location, DestVI, STdeconvolve) methods. For cell2location ($ARI = 0.31$) we used its built-in Leiden clustering; when inserting the BayesTME spatial clustering, cell2location improved to $ARI = 0.93$, suggesting the BayesTME clustering provides an independent benefit even for accurate deconvolution methods.

BayesTME accurately identifies the correct number of cell phenotypes and each phenotype expression signature. BayesTME is reference-free and thus uses the ST data to estimate the number of cell types and their signature, without the need for scRNA. There are two tunable hyperparameters in BayesTME: K , the number of cell types, and λ , the global degree of smoothness. BayesTME uses a spatial cross-validation approach to automatically select both variables without the need for user input. The cross-validation procedure creates m non-overlapping folds each with $\kappa\%$ of spots held out; we set $m = 5$ and $\kappa = 5\%$. For each fold, BayesTME enumerates $K = 2, \dots, K_{\max}$ and $\lambda = 10^1, \dots, 10^6$; in all of our experiments we set $K_{\max} = 15$. For each (K, λ) , we fit BayesTME on the in-sample data.

Graph smoothing priors enable BayesTME to fill-in missing spots during cross-validation. BayesTME uses these imputed posterior estimates to evaluate the likelihood on the held out data. BayesTME integrates out λ in order to select K then chooses the λ value closest to the mean held out likelihood for the chosen K ; see the Methods for details.

We evaluated how well the BayesTME cross-validation approach recovers the true cell type count in each of our K^* settings. We compared the BayesTME result to STdeconvolve, a reference-free alternative method based on latent Dirichlet allocation (Blei et al., 2003) that provides three different approaches to estimating the number of cell types; we picked the closest estimation out of the three candidates that STdeconvolve provided. Reference-based methods assume access to ground truth cell type information from scRNA annotation, making them unavailable for comparison. In each simulation, STdeconvolve over- or underestimated the true number of cell types whereas BayesTME selected the correct number of cell types (Figure 2c).

After determining the number of cell types, BayesTME infers the expression signature of each cell type directly from the ST data without needing access to scRNA or other reference signature data. Figure 2d shows the recovered expression signatures, cell type probabilities, and cell counts in the $K^* = 3$ simulation. Across all three variables, BayesTME recovered the ground truth with Pearson correlation $r^2 > 0.9$. Similar results on recovering expression signatures, cell counts, and cellular probabilities held across all our experiments; see the Supplement for results on other K^* settings.

BayesTME identifies within-phenotype spatial transcriptional programs with tight control of the false discovery rate. After deconvolution and cell typing, BayesTME augments its probabilistic model with one that allows gene expression levels of each phenotype to vary in space. To do this, BayesTME replaces the static Poisson phenotype likelihood with a negative binomial. The rate parameter in the negative binomial is set to the Poisson rate and the success probability is allowed to vary as a function of space. Hierarchical spatial shrinkage and clustering priors enable BayesTME to discover genes within each phenotype that spatially vary in coordination with other genes. We call these gene sets and spatial patterns *spatial transcriptional programs* (STPs). The STP construction in BayesTME is flexible: it allows for genes to be negatively spatially correlated within the same program, makes no assumption on the shape or pattern of spatial variation, and adaptively discovers how many genes are in each program. After inference, we use the posterior uncertainty to select STPs with control of the Bayesian false discovery rate (see Methods); we set the FDR target to 5% by default.

To benchmark BayesTME, we constructed a simulation dataset with spatial transcriptional programs by randomly sampling cells from the scRNA data following the same fashion as in the previous experiments. We used the spatial layout from a zebrafish melanoma sample as it is a large tissue containing more than 2000 spots, enabling a rich set of spatial patterns to be imprinted. We chose $K^* = 3$ cell types and designed 2 spatial programs for each cell type, where 10 genes were randomly sampled and assigned to each of the STPs (Figure 3 c). After selecting these 60 spatial genes, we reordered their sampled reads by the spot intensity of their respective spatial programs to simulate the spatial differentiation while preserving the mean expression. Thus, while the gene expression patterns are spatially informative in these simulations, clustering by scRNA-seq analysis would remain unchanged.

We benchmarked BayesTME against spatial differential expression methods (Svensson et al., 2018; Sun et al., 2020) that enable control of the false discovery rate. BayesTME identified all 6 spatial transcriptional programs with on average 0.88 Pearson's r correlation to the ground truth (Figure 3a,c). In contrast, we found SpatialDE and Spark could only detect cell-type proportion patterns instead of meaningful within-phenotype variation in spatial gene expression (Figure 3d-e). Quantitatively, BayesTME achieved an average false discovery proportion of 14% where the 95% confidence interval covers the 5% target FDR, and TPR of 94% for selecting spatially varying genes (Figure 3b).

BayesTME accurately corrects previously-unreported directional spot bleeding in ST data. Plots of raw UMI counts in real ST data (Figure 4e-g) show the UMI signal bleeds to background spots with a gradient of intensity. These plots also suggest, unlike the Gaussian assumption in previous preprocessing methods (Ni et al., 2021), or the uniform background noise model in other models (Kleshcheynikov et al., 2022), bleeding error varies in magnitude in different directions. Such phenomena may be the result of cell-free DNA from dead cells, mRNA binding capacity limitation of spatial barcodes, or technical artifacts of tissue permeabilization.

BayesTME corrects bleeding while preserving the true signal. To do this, BayesTME learns a semi-parametric anisotropic bleeding model to correct directional ST bleed and map UMIs to their most likely origin in the tissue. The BayesTME correction only assumes that UMI bleeding decays monotonically as a function of distance. Non-tissue regions are leveraged by BayesTME as a form of negative control, enabling the method to identify the underlying spatial error function from the data via a maximum likelihood estimation procedure.

To evaluate the performance of the BayesTME bleed correction, we constructed synthetic datasets simulating three different bleeding mechanisms: Gaussian, heavy-tailed multivariate-t, and anisotropic direction-biased bleeding (Figure 4b-d). The last simulation was constructed to resemble real ST data, with bias towards a specific corner of the slide. We compared BayesTME with SpotClean (Ni et al., 2021), an existing ST error correction technique that assumes Gaussian technical error. BayesTME achieved comparable performance in Gaussian ($\mu_{MSE,SpotClean} = 1170.08$, $\mu_{MSE,BayesTME} = 1263.66$, $p\text{-value} = 0.06$) and multivariate-t ($\mu_{MSE,SpotClean} = 1210.06$, $\mu_{MSE,BayesTME} = 1305.31$, $p\text{-value} = 0.69$) tasks, and outperformed SpotClean in anisotropic bleeding data ($\mu_{MSE,SpotClean} = 10437.48$, $\mu_{MSE,BayesTME} = 3048.92$, $p\text{-value} = 1.87 \times 10^{-301}$).

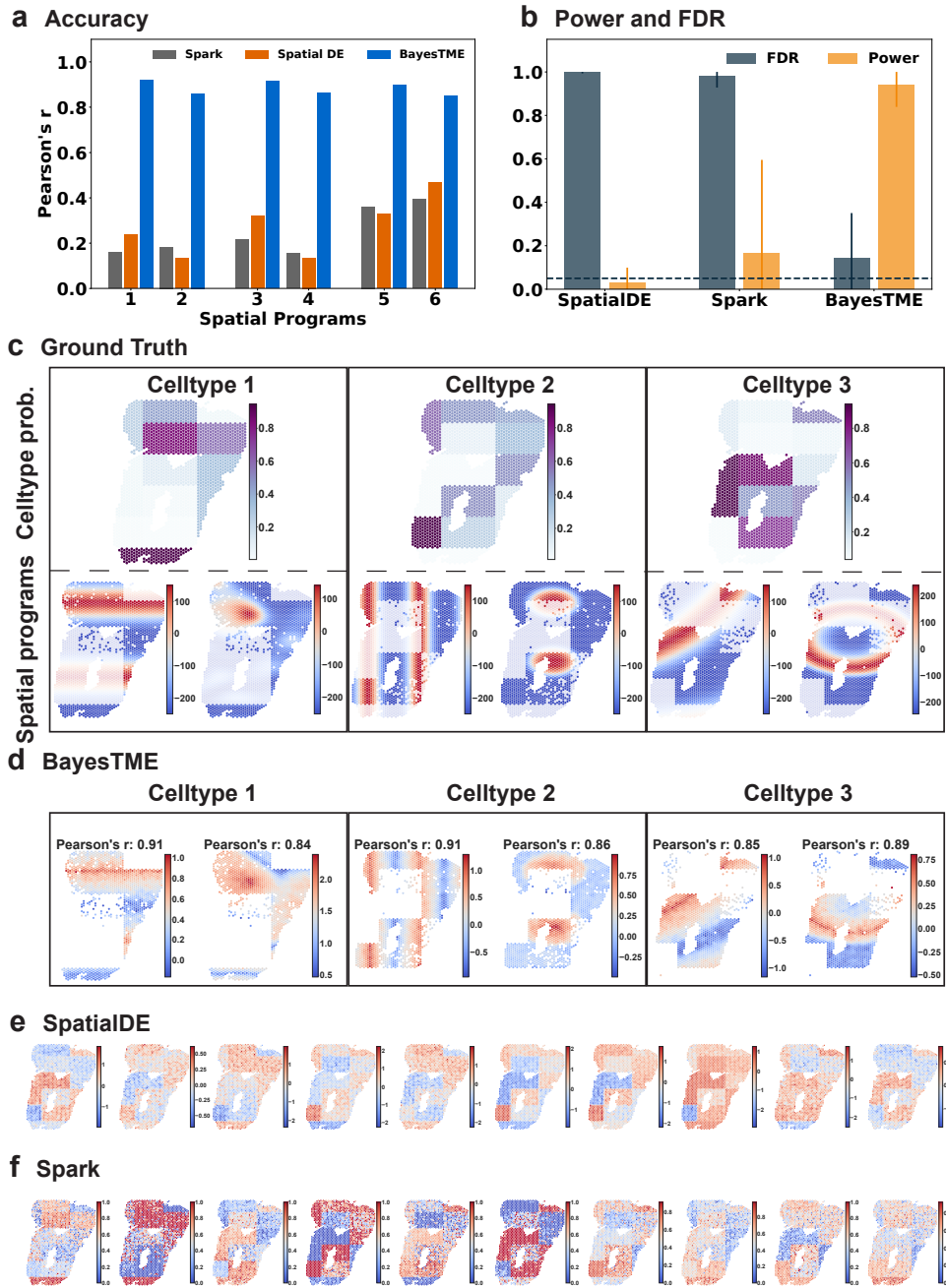


Figure 3: BayesTME discovers spatial transcriptional programs with high power and tight control of the false discovery rate (a.) Accuracy of the closest spatial pattern discovered by each method to the ground truth. (b.) True positive rate (orange) and false discovery rates for each method when predicting which genes belong to each spatially varying pattern; the dashed line is the target (5%) false discovery rate. (c.) Ground truth spatial patterns used in the benchmark simulations; top: cell type proportion probabilities; bottom: spatial pattern followed by the genes in each spatial program. (d.) Spatial programs found by BayesTME at the 5% FDR level. (e-f.) Spatial patterns found by other methods; both SpatialDE and Spark are unable to disentangle cell proportion from spatial gene expression within phenotypes.

We found that cell typing and deconvolution were robust to this spatial error. However, the preprocessing step was critical to preventing genes from falsely registering as spatially varying in real data experiments. These results suggest that ST workflows should take care to allow ample non-tissue space in each direction of the slide. If the tissue section exceeds the fiducial markers substantially in a given direction, the technical error function will be statistically unidentifiable. In such cases, it will be impossible to distinguish technical error from true spatial variation, potentially leading to false conclusions when assessing spatially-varying gene expression within-phenotypes.

BayesTME discovers novel spatial programs of immune infiltration and response in human melanoma. We applied BayesTME to a published human melanoma dataset (Thrane et al., 2018) generated using first generation ST technology, with a spot diameter of $100\ \mu m$ and center-to-center distance between spots of $200\ \mu m$ (Ståhl et al., 2016). The selected sample contained visible tumor, stromal, and lymphoid tissues as annotated by a pathologist based on H&E staining (Figure 5a). Despite the relatively low resolution of the data, the cell types identified by BayesTME successfully recapitulated the histology of the tissue (Figure 5b).

Five spatial transcriptional programs were identified by BayesTME (Figure 5c). Two programs were tumor-specific, and displayed somewhat distinct expression patterns, suggesting a spatially-segregated pattern of tumor heterogeneity (Figure 5c). As expected, melanoma marker genes such as *PMEI* and *SOX10* were highly upregulated within the tumor programs (Figure 5d). Similar to the pathologist annotations, the model also detected spatial programs corresponding to stromal (fibroblast) and lymphoid tissues (Figure 5c), which marker genes including *COL1A1* (fibroblast-specific, Figure 5c-d) and *CXCL13* (lymphoid-specific, Figure 5d). Notably, *MYL9* was one of the most highly expressed genes within the fibroblast expression signature (Figure 5d), which is a marker of tumor-associated myofibroblasts (Puram et al., 2017), indicating that the fibroblast program identified by BayesTME represents a subpopulation of fibroblasts reprogrammed by their proximity to the tumor. In the fibroblast-related spatial program, immune-related hub genes like *IGLL5* and *IGJ* displayed an enrichment at the tumor boundary (Figure 5c). The model also identified a macrophage-related spatial program (Figure 5c), which had not been detected by the pathologist. One of the top macrophage marker genes, *CXCL9* (Figure 5c-d) is a marker of tumor-associated macrophages (Marcovecchio et al., 2021), which have an important role in anti-tumor immunity (Chow et al., 2019). Taken together, our results show that BayesTME can successfully not only recapitulate, but also improve the detection of novel tumor and tumor-associated cell types that are difficult to identify purely by histology.

BayesTME discovers spatial programs capturing muscular bilateral symmetry and tumor-immune interaction in a zebrafish melanoma model. We expanded upon our human melanoma results by applying BayesTME to our recently published dataset of zebrafish *BRAF^{V600E}*-driven melanoma (Hunter et al., 2021), generated using the 10X Genomics Visium technology with approximate spot resolution of $55\ \mu m$. Both samples contained tumor and TME tissues (muscle, skin) (Figure 6, Figure 7).

Within Sample A, BayesTME identified four cell types corresponding to tumor, muscle and skin (Figure 6b-c). Each cell type upregulated expected marker genes, such as myosins and parvalbumins in muscle (*myhc4*, *myl10*, *pvalb1*, *pvalb2*, *pvalb3*, *pvalb4*), *BRAF^{V600E}* in tumor, and keratins in skin (*krt5*, *krt91*, *krt15*) (Figure 6c). Two celltypes (“Tumor” and “Interface”) were detected within the tumor, both expressing *BRAF^{V600E}* (Figure 6a-c). Although the tumor region of Sample A bordered adjacent muscle with little mixing of the two tissue types visible on the H&E-stained section , the interface cell type appeared to infiltrate into the neighboring TME, reminiscent of the interface cell we identified in our recent work (Hunter et al., 2021) (Figure 6a). Many of the interface marker genes were the same as interface marker genes we previously identified, including *stmn1a*, *tubb2b*, and *hmga1a* (Hunter et al., 2021) (Figure 6c). Both spatial programs corresponding to the interface type were enriched at the tumor boundary (Figure 6d). In addition to the interface marker genes we previously identified, BayesTME uncovered a number of genes related to remodeling of the extracellular matrix (ECM) that displayed a spatial enrichment at the tumor boundary, including several collagen-related genes (*col1a1a*, *col1a2*, *col1a1b*; Figure 6d), consistent with a role for the interface cell state in melanoma invasion. Immune genes were also enriched at the tumor-muscle interface,

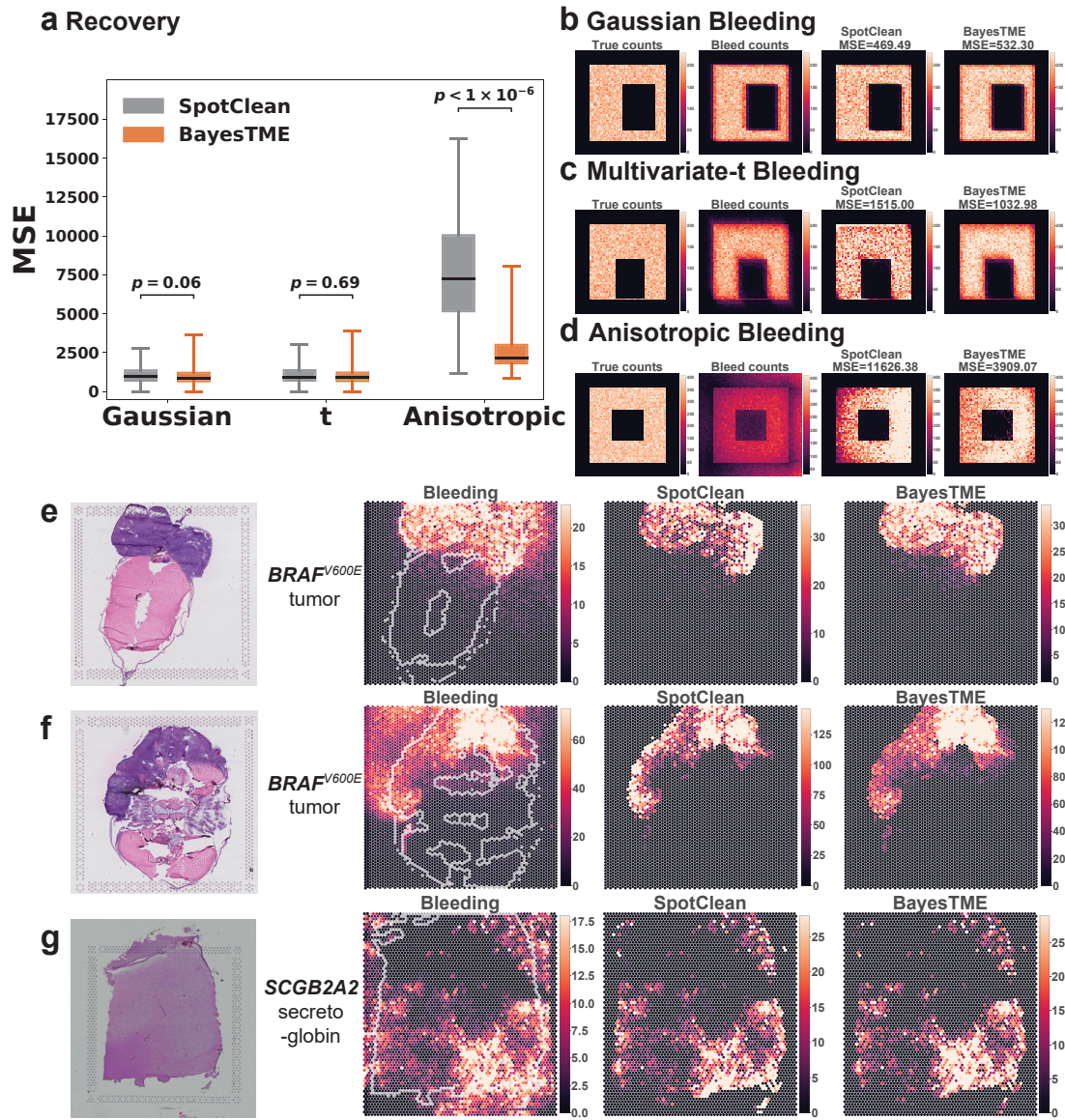


Figure 4: BayesTME recovers UMI reads from bleeding contamination and preserves the spatial pattern of interest. (a.) BayesTME performs similarly to SpotClean when the bleeding pattern is isotropic (Gaussian or Student's t); BayesTME substantially outperforms SpotClean when bleeding skews UMIs toward one direction. (b-d.) Examples of simulated bleeding patterns showing how BayesTME is able to learn and correct for the direction of the bleeding pattern in the anisotropic case. (e-g.) Bleed correction of selected marker genes in (e.) zebrafish sample A, (f.) zebrafish sample B, and (g.) human dorsolateral prefrontal cortex, with comparison to SpotClean. Bleeding patterns consistently show anisotropic skew towards one corner. SpotClean UMI corrections are therefore expected to be biased towards the tissue boundary whereas BayesTME is more diffuse and better recapitulates the true signal.

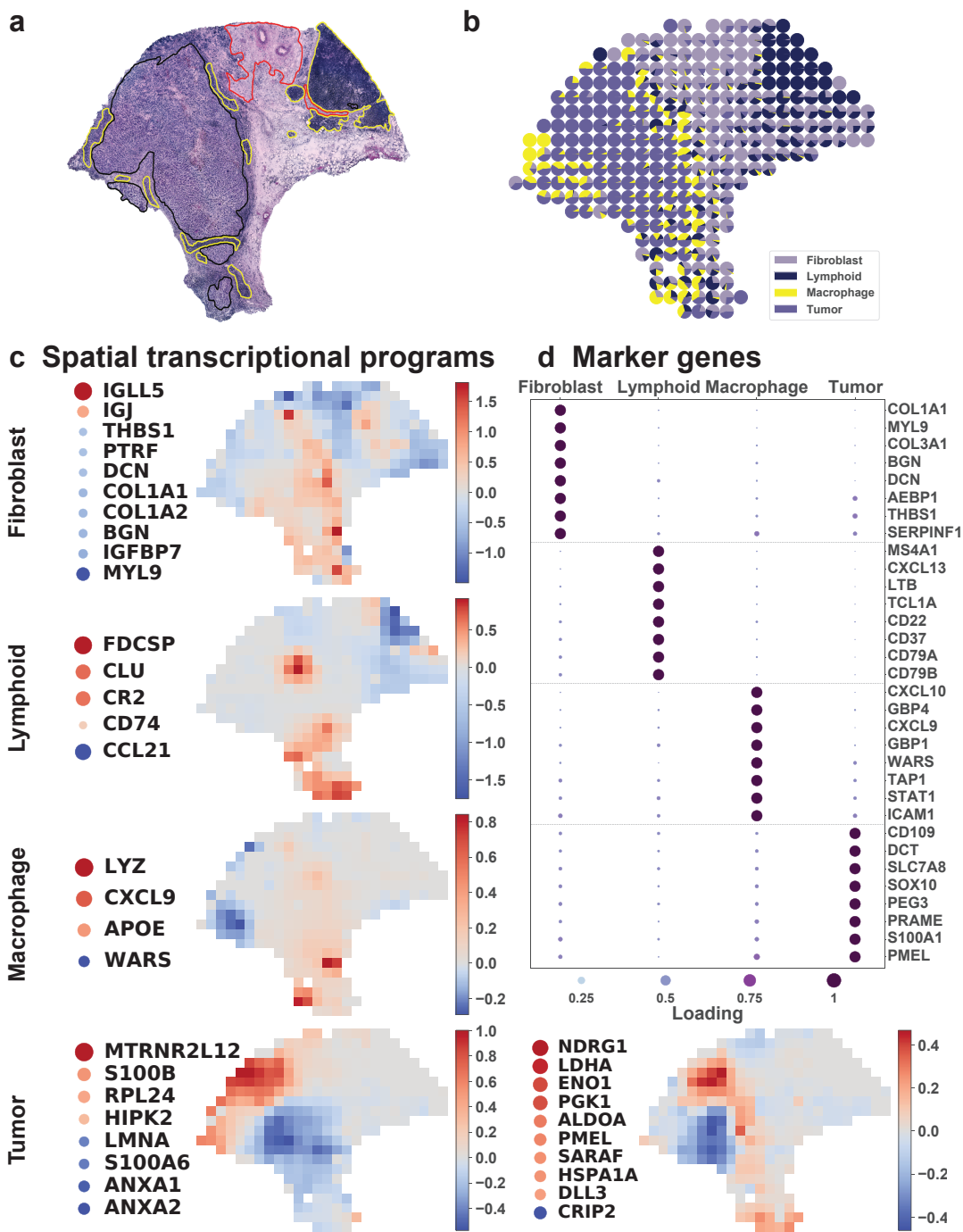


Figure 5: BayesTME discovers novel spatial programs of immune-tumor interaction in human melanoma. (a.) Pathologist-annotated H&E slide; yellow: immune cells, red: stroma, black: tumor. (b.) BayesTME recovers 4 cell types which map closely to the pathologist annotations. (c.) BayesTME recovers 5 spatial programs representing fibroblasts, immune cells, and two programs covering tumor subtypes related to transcription (left) and stress responses (right). (d.) Top marker genes selected by BayesTME to describe each cell type.

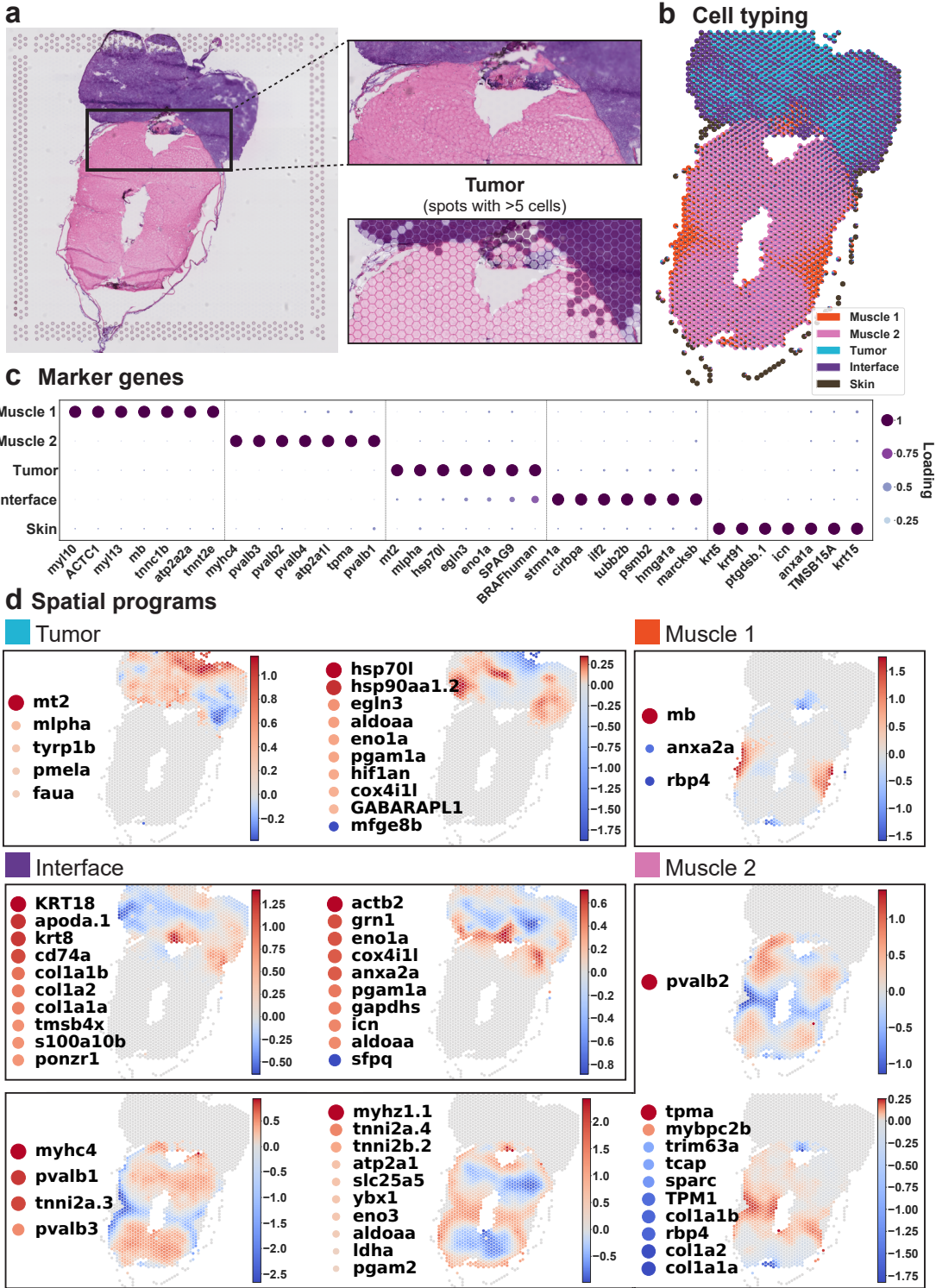


Figure 6: BayesTME identifies sharp boundaries and novel tumor interface programs in a zebrafish melanoma model. (a.) Histology of zebrafish sample A; cutout: zoom in on the tumor interface region. (b-c.) BayesTME discovers 5 cell phenotypes with biologically plausible marker genes; cutout: zoom in on the recovered tumor/not-tumor proportions show BayesTME captures the sharp tissue change point. (d.) 9 spatial transcriptional programs discovered at a 5% FDR; muscle programs illustrate BayesTME captures bilateral symmetry without prior knowledge; interface and tumor programs capture differences between interior and exterior tumor behavior.

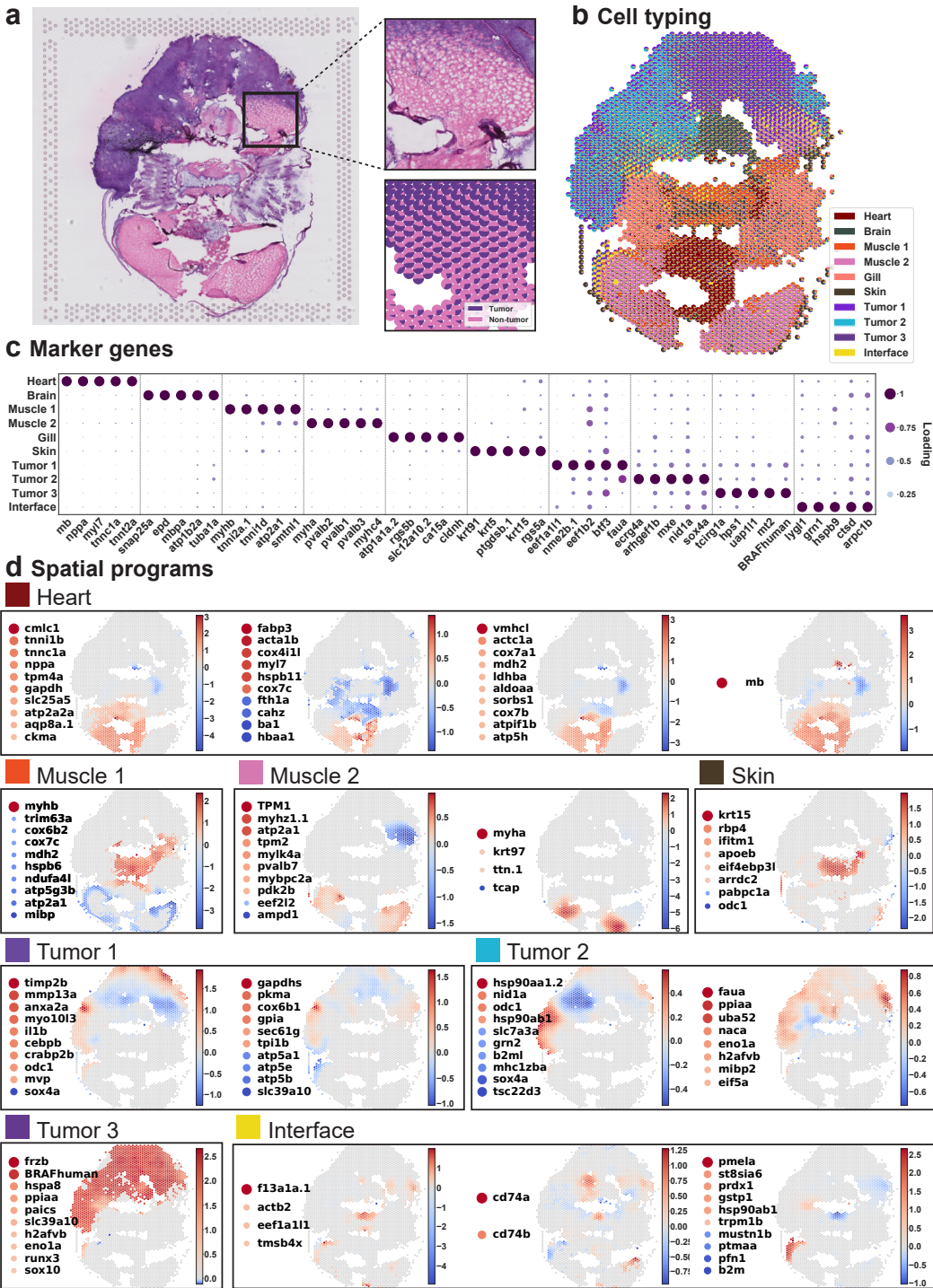


Figure 7: BayesTME reveals gradual tumor invasion and confirms interface programs in a second zebrafish melanoma model **(a.)** Histology of the zebrafish B sample; cutout: tumor interface with gradual invasion of tumor cells into the muscle region. **(b.)** BayesTME cell types recovered; cutout: corresponding tumor-muscle interface with tumor/non-tumor proportions capturing the gradient of tumor invasion present in histology. **(c.)** Marker genes for the discovered 10 cell types. **(d.)** 16 spatial transcriptional programs discovered at a 5% FDR.

including *ilf2* and *grn1* (Figure 6c-d).

Sample B contains a wider variety of tissue types including heart, brain, gills, tumor, and muscle (Figure 7a-c). Mixing of tumor and muscle tissues at the tumor boundary was visible by histology (Figure 7a). Notably, BayesTME again uncovered an “interface” cell state specifically enriched at the tumor boundary (Figure 7a-b). Similar to Sample A, a number of immune-related genes were spatially patterned and/or enriched in the interface region, including *lygl1*, *grn1*, *cd74a/b*, and *b2m* (Figure 7c-d). Melanoma is a highly immunogenic cancer whose interaction with immune cells in the TME significantly influences tumor progression (Passarelli et al., 2017). Whether the enrichment of immune genes at the tumor-TME interface represents pro-inflammatory tumor cells at the tumor boundary, or a type of novel tumor-associated immune cell type will be an exciting topic of future investigation.

In both samples, we uncovered a significant degree of spatially-patterned tumor heterogeneity. BayesTME identified spatial programs characterized by up-regulation of classical melanoma markers such as *pmla* and *tyrp1b* (Sample A “Tumor”, Figure 6d) and *BRAF^{V600E}* and *sox10* (Sample B “Tumor 3”, Figure 7d). Other spatial programs identified in the tumor likely represent other facets of tumor biology. Hypoxia-related genes (*hif1an*, *egln3*; Figure 6d) were spatially enriched within the tumor region of Sample A, which may indicate hypoxic regions of the tumor due to lack of oxygen supply. Hypoxia has been linked to melanoma progression (Huber et al., 2016). We also identified spatially-patterned signatures of metabolism, which could represent different metabolic pathways active within the tumor. One of the spatial programs identified within the tumor region of Sample B up-regulated several genes corresponding to ATP synthase subunits (*atp5a1*, *atp5e*, *atp5b*) and other metabolic genes (*gpla*, *tpi1b*) (Figure 7d). Determining how different metabolic pathways are spatially-organized and regulated within the tumor will be an interesting area of further study. Taken together, our results indicate that BayesTME identifies complex spatial patterns of transcriptional heterogeneity within melanoma and the melanoma microenvironment, and uncovers a potentially novel pro-inflammatory cell state present at the tumor boundary.

3 Discussion

This paper has presented BayesTME, a reference-free Bayesian method for end-to-end analysis of spatial transcriptomics data. BayesTME first corrects for anisotropic technical error that has been unreported in previous ST analyses. BayesTME then deconvolves ST data into distinct cell types, identifies expression signatures of each cell type, and detects spatial transcriptional programs automatically without any scRNA-seq reference. BayesTME was shown to outperform a suite of methods on benchmarks for technical error correction, spot deconvolution, and cellular community detection. In human and zebrafish tissues, BayesTME discovered spatial transcriptional programs that revealed insights into how subsets of genes coordinate in tumor and healthy tissue at different points.

Compared with existing scRNA-seq referenced methods, BayesTME applies to a wider variety of tissues as scRNA-seq may not be tractable due to economic, technical, or biological limitations. However, BayesTME is adaptable to scRNA-seq reference if available. With reference data, one can obtain the empirical estimation of the expression signature ϕ , which is invariant to sequencing depth batch effects. Computationally, access to pre-clustered scRNA-seq significantly accelerates the inference by removing the need to perform cross-validation to select the cell phenotypes. On the other hand, unlike most reference-free methods, BayesTME does not rely on dimension reduction like PCA. This advantage enables BayesTME to draw individual gene-level inferences including expression signatures, phenotype markers, and spatial transcriptional programs.

Advances in ST technology promise to soon enhance the resolution to near-single cell levels, dramatically increasing the number of spots. We have carefully designed the computational inference routines in BayesTME to meet this challenge. BayesTME scales sub-linearly with the number of spots, with a 100x increase in the number of spots leading to only a 10x increase in computational runtime (Supplementary Fig. 2). To further speed up inference, one can place an informative prior on the cell count in a given spot using the H&E slide as reference; simulation experiments show that with a handful of noisy cell count annotations, the cell count accuracy also improves to nearly perfect (see the Supplement for details).

Understanding how cells alter their expression levels as a function of their spatial location in a tissue

is necessary for a complete characterization of the cellular architecture of the tissue microenvironment. BayesTME captures these expression level changes in the form of spatial transcriptional programs. Our results showed BayesTME is able to capture biologically meaningful spatial programs which hint at cell-cell interaction in tumor microenvironments. To further facilitate our understanding of cell-cell interaction mechanisms, future versions of BayesTME will introduce an additional cell-type interaction term in the success rate formulation in our negative binomial model. This interaction term will model the total influence cell type k in spot i as the sum of the interactions between cell type k and all possible cell types k' . We also plan to explore extending this formulation to all spots within a reasonable neighboring of spot i for global interactions triggered by paracrine, synaptic, or endocrine signaling. This process is computationally expensive under the current ST technology. However, with single-cell resolution, such inference becomes tractable as we only need to look at the individual cells of different cell types within the reasonable neighborhood of cell i . Increased ST resolution will significantly drop the computation cost by a factor of K , which can also be vectorized to further speed up this process. Thus, BayesTME is well-positioned to make future computational advances in ST modeling, in step with the coming technological advances in ST methods.

4 Method

4.1 Notation and setup

We assume we are given an $N \times G$ matrix R where R_{ig} is the UMI counts for gene g at spot i . The spot i is associated with some known location $l(i) \in \mathbb{R}^2$ on the tissue. These locations define a graph $\mathcal{G} = (\mathcal{V}, \mathcal{E})$ where each vertex is a spot. There is an edge between two vertices if they are within some ϵ distance. We set $\epsilon = \sqrt{2}$ such that each non-boundary spot has 4 neighbors for lattice layouts (e.g., Slide-seq) and 6 neighbors for hexagonal layouts (e.g., Visium). We assume that there are K cell phenotypes (hereon simply called cell types) in the sample, each with their own expression profile. We do not assume that K is known nor do we assume that there is side information about different cell types and their expression profiles (i.e., we do not assume access to paired single-cell RNA). We refer to UMI counts and read counts interchangeably, where read counts are understood to mean UMI-filtered reads and not raw, possibly-duplicated reads.

4.2 Gene selection

BayesTME scales linearly with the size of the gene library. To keep posterior inference computationally tractable, we select the top $G = 2000$ genes ordered by spatial variation in log space. Specifically, we transform the reads as $\log(1+R)$ and rank each column by the variance, keeping the top 2000. The logarithmic transform separates spatial variation from natural variation that arises due to simply having a higher overall expression rate. We then drop all ribosomal genes (i.e., those matching an ‘rp’ regular expression). After selecting and filtering the top genes, we work directly with the UMI read counts.

4.3 Anisotropic bleed correction

Technical error causes UMIs to bleed out from wells. BayesTME models this bleed as a combination of unknown global and local effects. Global effects form a baseline bleed count for any spot, corresponding to a homogeneous diffusion process. Local effects imply that the UMI count at a given spot is a function of how far it is from the original location of each of the UMIs. BayesTME employs a semi-parametric, anisotropic

model for global and local effects,

$$\begin{aligned}\tilde{\mathbf{R}}_g &\sim \text{Mult} \left(\sum_i \tilde{R}_{ig}, \boldsymbol{\rho}_g / \sum_i \rho_{ig} \right) \\ \rho_{ig} &= \rho_{0g} + \sum_{i'} w_{ii'} \mu_{i'g} \\ w_{ii'} &= \sum_{b=1}^B \sum_{j=0}^{s_b(i,i')} \log(1 + e^{\zeta_{bj}}),\end{aligned}\tag{1}$$

where $\tilde{\mathbf{R}}_g$ are the raw, observed counts and ρ_{0g} are the global effects. The local effects in [Equation \(1\)](#) are modeled using a set of B monotone nonparametric basis functions ζ that decay as a function of the basis-specific pseudo-distance s_b .² BayesTME uses the four cardinal directions (North, South, East, and West) for the basis functions. This choice is based on the observation that UMIs tend to bleed toward one corner. We also observed that bleeding appears to be less extreme in tissue regions than non-tissue regions. Thus, BayesTME distinguishes between in- and out-of-tissue distance by learning four separate basis functions for each region. The distance from an original spot i' to its observed spot i is then a summation of the in- and out-of-tissue components of a straight line between the two spots.

The bleeding model is fit by alternating minimization. At each iteration, BayesTME alternates between estimating the basis functions ζ and global rates $\hat{\rho}_{0g}$, and estimating the latent true UMI rates $\hat{\mu}_{ig}$. After the model is fit, BayesTME replaces the raw reads with the approximate maximum likelihood estimate of read counts,

$$R_g = \arg \max \text{Mult} \left(R_g; \sum_i \tilde{R}_{ig}, \hat{\boldsymbol{\rho}}_g / \sum_i \hat{\rho}_{ig} \right) \approx \text{round} \left(\tilde{R}_{ig} \times \hat{\boldsymbol{\rho}}_g / \sum_i \hat{\rho}_{ig} \right). \tag{2}$$

The cleaned reads R are then treated as correct in subsequent inference steps. This can be seen as an empirical Bayes approach, where the model in [Equation \(1\)](#) is optimized and uncertainty over R is replaced with a point estimate that maximizes the marginal likelihood of possible true read configurations.

4.4 Discrete deconvolution model

The spot-wise gene counts R_{ig} can be decomposed into the sum of cell type-specific gene reads in any given spot, i.e. $R_{ig} = \sum_{k=1}^K R_{igk}$. BayesTME models the cell type-specific reads with a Poisson distribution controlled by three parameters β_k , d_{ik} and ϕ_{kg} . Specifically, β_k denotes the expected total UMI count of individual cells of type k ; d_{ik} denotes the number of cells of type k located in spot i ; and $\phi_k = (\phi_{k1}, \dots, \phi_{kG})$ denotes the gene expression profile of cell type k , where each element ϕ_{kg} is the normalized expression of gene g in cell type k ; equivalently, ϕ_{kg} is the proportion of UMIs that cell type k allocates to gene g . The generative model for BayesTME follows,

$$\begin{aligned}R_{ig} &= \sum_{k=1}^K R_{igk} \\ R_{igk} &\sim \text{Pois}(\beta_k d_{ik} \phi_{kg}) \\ \boldsymbol{\phi}_k &\sim \text{Dir}(\boldsymbol{\alpha}) \\ \beta_k &\sim \text{Gamma}(a, b) \\ D_i &\sim \text{Binom}(n_{max}, 1 - \sigma(\psi_{i0})) \\ d_{ik} &\sim \text{Binom}(n_{k-1}, \sigma(\psi_{ik})), \quad \forall 1 < k < K \\ (\Delta\Psi)_j &\sim \text{GroupHorseshoe}(\lambda)\end{aligned}\tag{3}$$

²Technically these basis functions are pseudo-distances as they do not satisfy symmetry and thus are not metric functions.

where D_i is the total number of cells in spot i , and λ is the hyperparameter that controls the degree of spatial smoothing. The matrix Δ is the edge-oriented adjacency matrix encoding the spot graph \mathcal{G} , also equivalent to the square root of the graph Laplacian. The hierarchical prior encoded by the last three lines of Equation (3) is a heavy-tailed Bayesian variant of the graph-fused group lasso prior (Faulkner and Minin, 2018; Tansey et al., 2017) that uses the Horseshoe+ distribution (Bhadra et al., 2017). This prior encourages the probability distribution over cell type proportions to follow a piecewise constant spatial function, encoding the prior belief that cells form spatially contiguous communities. The model is data-adaptive, however, and able to handle deviations from this prior where warranted in the data; see for example, the smooth gradient of cell type proportions recovered in Figure 7.

4.5 Posterior inference

Posterior inference in BayesTME is performed through Gibbs sampling. The full derivations for all complete conditionals and update steps are available in the supplementary material. The key computational innovations in BayesTME come in the form of a fast approach to update d_{ik} , the number of cells of type k in spot i . As we show in the supplement, block joint sampling over all \mathbf{d}_i and D_i can be done via an efficient forward-backward algorithm. This algorithm effectively converts the cell count prior to a hidden Markov model prior. The Poisson likelihood in Equation (3) acts as the emissions step and the emission log-likelihood can be collapsed into a series of fast updates. This inference step enables us to sample over the entire combinatorial space of possible cell counts in $\mathcal{O}(ND_{\max}^2 K^2)$ time for N spots, K cell types, and $0 \leq D_i \leq D_{\max}$ possible total cells in each spot. BayesTME performs Gibbs sampling using these fast updates with a burn-in and Markov chain thinning; we use 2000 burn-in steps, 5 thinning steps between each sample, and gather a total of $T = 100$ post-burn-in posterior samples.

4.6 Selecting the number of cell types and smoothness hyperparameters

BayesTME automatically chooses the number of cell types K via M -fold cross-validation. For each fold, a random non-overlapping subset of the spots are held out; we use $M = 5$ folds with 5% of spots held out in each fold. The spatial priors in BayesTME enable imputation of the cell type probabilities at each held out spot in the training data. For each fold, we fit over a discrete grid of λ smoothness values; we use $\lambda = (10^0, 10^1, \dots, 10^6)$. For a given fold m , cell type count K , and smoothness level λ , we calculate the approximate marginal log-likelihood of the held out spots,

$$\mathcal{L}^{\text{test}} = \sum_{i \in \text{fold}_m} \sum_{t=1}^T \log \text{Mult} \left(\mathbf{R}_i; \sum_g R_{ig}, \frac{\sum_k \beta_k^{(t)} \theta_{ik}^{(t)} \phi_k^{(t)}}{\sum_g \sum_k \beta_k^{(t)} \theta_{ik}^{(t)} \phi_{kg}^{(t)}} \right). \quad (4)$$

Results are averaged over all λ values for each fold and then averaged across each fold. The λ averaging is an empirical Bayes estimate with a discrete prior on λ integrated out; the cross-validation averaging is an unbiased approach to selecting K . After selecting K , we refit BayesTME on the entire data using the chosen K and the λ with average cross-validation log-likelihood closest to the overall average.

4.7 Selecting marker genes

We define a gene as a marker of a particular cell type if its expression in that cell type is significantly higher than in any other cell type. BayesTME uses posterior uncertainty to select statistically significant marker genes with control of the Bayesian false discovery rate (FDR) (Efron, 2012). To calculate the local FDR we use the T posterior samples,

$$\omega_{kg} = 1/T \sum_{t=1}^T \prod_{k' \neq k} \mathbb{1} [\phi_{kg} > \phi_{k'g}], \quad (5)$$

yielding the posterior probability that gene g is a marker for cell type k . We sort the ω values in descending order and solve a step-down optimization problem,

$$\begin{aligned} & \underset{q}{\text{maximize}} && q \\ & \text{subject to} && \frac{\sum_{i=1}^q (1 - \omega_{(i)})}{q} \leq \alpha. \end{aligned} \tag{6}$$

The set of ω values selected controls the Bayesian FDR at the α level. BayesTME can alternatively control the Bayesian Type I error rate at the α level by only selecting marker genes satisfying $\omega_{kg} \geq 1 - \alpha$. By default, we set the FDR threshold to 5%; our results report an interpretable subset of the top 20 genes for each inferred cell type.

4.8 Community detection

To segment the tissue into cellular communities, BayesTME clusters the fused spatial probabilities Ψ . First, the neighbor graph is augmented with the nearest 10 neighbors to adjust for spatially-disconnected spots due to tissue tears in sectioning. The posterior samples are flattened into a single vector for each spot. Spots are then clustered using agglomerative clustering with Ward linkage, as implemented in `scikit-learn`. The number of clusters q is chosen over a grid of $q \in (1, \dots, 50)$ to minimize the sum of the AIC (Sakamoto et al., 1986) and BIC (Neath and Cavanaugh, 2012) scores. Community distributions are calculated as the average of all posterior probabilities of all spots assigned to the community. When comparing community segmentation in benchmarks, we applied BayesTME’s clustering algorithm on DestVI and stDeconvolve, as they do not provide segmentation routines.

4.9 Spatial transcriptional program model

The deconvolution model in Equation (3) assumes gene expression is stationary within a given cell type. However, we expect that variation in a small number of important genes should be spatially dependent. BayesTME captures this spatial variation by replacing the Poisson likelihood in Equation (3) with a more complex negative binomial one,

$$\begin{aligned} R_{igk} &\sim NegBinom(\beta_k d_{ik} \phi_{kg}, \sigma(w_{ki}^{(h_{kg})} v_{kg} + c_{kg})) \\ h_{kg} &\sim Cat(\theta_k) \\ \theta_k &\sim Dirichlet(10, 1, 1, \dots, 1) \\ c_{kg} &\sim \mathcal{N}(0, 1) \\ v_{kg} &\sim Horseshoe+ \\ w_k^{(0)} &= \mathbf{0} \\ (\Delta^{(1)} w_k^{(h>0)})_j &\sim Horseshoe+, \end{aligned} \tag{7}$$

where σ is the logistic function and $\Delta^{(1)} = \Delta^T \Delta$ is the first-order graph trend filtering matrix, equivalent to the graph Laplacian. The rate in Equation (7) is equivalent to that in the simpler model in Equation (3). In both cases, the expected read count scales additively with the number of cells, a crucial property that reflects the intuition that a spot with twice as many cells should yield twice as many reads.

Gene expression within a cell type varies spatially through the success probability (the second term) in the negative binomial likelihood. The offset term c_{kg} corresponds to the spatially-invariant expression term that controls the dispersion rate in the counts. Each gene g in each cell type k belongs to one of H clusters. Each cluster defines a different spatial pattern $\mathbf{w}_k^{(h)}$, which we refer to as *spatial transcriptional programs*. The first program $\mathbf{w}_k^{(0)}$ is the null program corresponding to spatially-invariant expression. All subsequent programs are latent and inferred through posterior inference. BayesTME places a heavy prior on genes coming from the null, such that it takes substantial evidence to conclude that a gene is spatially varying within a cell

type; this prior is necessary as otherwise the model is only weakly identifiable. Genes that participate in the non-null spatial programs do so by placing a weight v_{kg} on the spatial pattern. This weight shrinks, magnifies, or can even invert the pattern, allowing for clustering of negatively correlated genes into the same spatial transcriptional program. BayesTME places a sparsity-inducing prior on v_{kg} in order to encourage only strongly-participating genes to be assigned to non-null programs.

4.10 Spatial transcriptional program inference

Posterior inference via Gibbs sampling is possible with the STP BayesTME model. However, the fast HMM updates for the cell counts are no longer available, making the inference algorithm substantially slower. For computational efficiency, we instead take a two-stage approach. First, we fit the deconvolution model in [Equation \(3\)](#), collecting T posterior samples of each latent variable. Then we fix $(\beta, \mathbf{d}, \Phi)^{(t)}$ for each sample $t = 1, \dots, T$. For each fixed sample, we run a new Gibbs sampler for the non-fixed variables in [Section 4.9](#); we use 99 burn-in iterations and take the 100th iteration as the sample for the t^{th} iteration of the full model parameters. We motivate this approach mathematically by the identity that if $Y \sim \text{Pois}(r)$ and $X \sim \text{NegBinom}(r, p)$ then $\mathbb{E}[Y] = \mathbb{E}[X \mid p = 0.5]$. Since we put sparsity priors on v_{kg} and a standard normal prior on c_{kg} , all of our priors are peaked at $p = 0.5$. Thus, *a priori*, we expect the posterior mean under the full joint inference model to be nearly the same as the two-stage model; in practice, we find the two approaches produce similar results.

4.11 Selecting significant spatial transcriptional programs

Spatial transcription programs in BayesTME correspond to spatial patterns in $w_k^{(h)}$ in cell type k and the members of a spatial program are the genes g for which h_{kg} is significantly non-null. Spatial programs are only considered active in spots i where $d_{ik} > 0$ with high probability. Specifically, for a given α significance level, we select spots and genes for spatial program s in cell type k as follows,

$$\begin{aligned}\mathcal{S}_{sk}^{\text{genes}}(\alpha) &= \left\{ v_{kg} : \left(\frac{1}{T} \sum_{t=1}^T \mathbb{1}[h_{kg}^{(t)} = s] \right) \geq 1 - \alpha \right\} \\ \mathcal{S}_{sk}^{\text{spots}}(\alpha) &= \left\{ w_{ki}^{(s)} : \left(\frac{1}{T} \sum_{t=1}^T \mathbb{1}[d_{ik}^{(t)} > 0] \right) \geq 1 - \alpha \right\}.\end{aligned}\tag{8}$$

If either $\mathcal{S}_{sk}^{\text{genes}}(\alpha)$ or $\mathcal{S}_{sk}^{\text{spots}}(\alpha)$ is empty, we filter out the entire program. We also filter any programs where the Pearson correlation between $w_k^{(h)}$ and d_k is more than 0.5 and Moran's I spatial autocorrelation less than 0.9; these programs capture technical noise and overdispersion rather than meaningful spatial signal. In practice, we find $H = 10$ to be a sufficient number of potential spatial programs per cell type. BayesTME sets the spatial transcriptional program significant threshold to $\alpha = 0.95$.

References

- Anusha Kalbasi and Antoni Ribas. Tumour-intrinsic resistance to immune checkpoint blockade. *Nature Reviews Immunology*, 20(1):25–39, 2020.
- Roy S Herbst, Jean-Charles Soria, Marcin Kowanetz, Gregg D Fine, Omid Hamid, Michael S Gordon, Jeffery A Sosman, David F McDermott, John D Powderly, and Scott N Gettinger. Predictive correlates of response to the anti-PD-L1 antibody MPDL3280A in cancer patients. *Nature*, 515(7528):563–567, 2014.
- Thomas F Gajewski, Seng-Ryong Woo, Yuanyuan Zha, Robbert Spaapen, Yan Zheng, Leticia Corrales, and Stefani Spranger. Cancer immunotherapy strategies based on overcoming barriers within the tumor microenvironment. *Current Opinion in Immunology*, 25(2):268–276, 2013.

Stefani Spranger, Robbert M Spaapen, Yuanyuan Zha, Jason Williams, Yuru Meng, Thanh T Ha, and Thomas F Gajewski. Up-regulation of PD-L1, IDO, and Tregs in the melanoma tumor microenvironment is driven by CD8+ T cells. *Science Translational Medicine*, 5(200):200ra116–200ra116, 2013.

Alessia Echarti, Markus Hecht, Maike Büttner-Herold, Marlen Haderlein, Arndt Hartmann, Rainer Fietkau, and Luitpold Distel. CD8+ and regulatory T cells differentiate tumor immune phenotypes and predict survival in locally advanced head and neck cancer. *Cancers*, 11(9):1398, 2019.

Nicholas Navin, Jude Kendall, Jennifer Troge, Peter Andrews, Linda Rodgers, Jeanne McIndoo, Kerry Cook, Asya Stepansky, Dan Levy, and Diane Esposito. Tumour evolution inferred by single-cell sequencing. *Nature*, 472(7341): 90–94, 2011.

10x Genomics. 10x Genomics: Visium spatial gene expression, 2022. URL <https://www.10xgenomics.com/products/spatial-gene-expression>.

Sanja Vickovic, Gökcen Eraslan, Fredrik Salmén, Johanna Klughammer, Linnea Stenbeck, Denis Schapiro, Tarmo Äijö, Richard Bonneau, Ludvig Bergenstråhle, José Fernández Navarro, Joshua Gould, Gabriel K. Griffin, Åke Borg, Mostafa Ronaghi, Jonas Frisén, Joakim Lundeberg, Aviv Regev, and Patrik L. Ståhl. High-definition spatial transcriptomics for *in situ* tissue profiling. *Nature Methods*, 16(10):987–990, 2019.

Samuel G Rodrigues, Robert R Stickels, Aleksandrina Goeva, Carly A Martin, Evan Murray, Charles R Vanderburg, Joshua Welch, Linlin M Chen, Fei Chen, and Evan Z Macosko. Slide-seq: A scalable technology for measuring genome-wide expression at high spatial resolution. *Science*, 363(6434):1463–1467, 2019.

Zijian Ni, Aman Prasad, Shuyang Chen, Richard B. Halberg, Lisa Arkin, Beth Drolet, Michael Newton, and Christina Kendziora. SpotClean adjusts for spot swapping in spatial transcriptomics data. *bioRxiv*, 2021. doi: 10.1101/2021.06.11.448105. URL <https://www.biorxiv.org/content/early/2021/07/28/2021.06.11.448105>.

Edward Zhao, Matthew R Stone, Xing Ren, Jamie Guenthoer, Kimberly S Smythe, Thomas Pulliam, Stephen R Williams, Cedric R Uytingco, Sarah EB Taylor, Paul Nghiem, Jason H Bielas, and Raphael Gottardo. Spatial transcriptomics at subspot resolution with bayesspace. *Nature Biotechnology*, pages 1–10, 2021.

Duy Pham, Xiao Tan, Jun Xu, Laura F. Grice, Pui Yeng Lam, Arti Raghubar, Jana Vukovic, Marc J. Ruitenberg, and Quan Nguyen. stlearn: integrating spatial location, tissue morphology and gene expression to find cell types, cell-cell interactions and spatial trajectories within undissociated tissues. *bioRxiv*, 2020. doi: 10.1101/2020.05.31.125658. URL <https://www.biorxiv.org/content/early/2020/05/31/2020.05.31.125658>.

Ruben Dries, Qian Zhu, Rui Dong, Chee-Huat Linus Eng, Huipeng Li, Kan Liu, Yuntian Fu, Tianxiao Zhao, Arpan Sarkar, Feng Bao, Rani E. George, Nico Pierson, Long Cai, and Guo-Cheng Yuan. Giotto: a toolbox for integrative analysis and visualization of spatial expression data. *Genome biology*, 22(1):1–31, 2021.

Brendan Francis Miller, Lyla Atta, Arpan Sahoo, Feiyang Huang, and Jean Fan. Reference-free cell-type deconvolution of pixel-resolution spatially resolved transcriptomics data. *bioRxiv*, 2021.

Romain Lopez, Baoguo Li, Hadas Keren-Shaul, Pierre Boyeau, Merav Kedmi, David Pilzer, Adam Jelinski, Eyal David, Allon Wagner, Yoseph Addadi, Michael I Jordan, Ido Amit, and Nir Yosef. Destvi identifies continuums of cell types in spatial transcriptomics data. *Nature Biotechnology*, pages 1–10, 2022.

Vitalii Kleshchevnikov, Artem Shmatko, Emma Dann, Alexander Aivazidis, Hamish W. King, Tong Li, Rasa Elmentaitė, Artem Lomakin, Veronika Kedlian, Adam Gayoso, Mika Sarkin Jain, Jun Sung Park, Lauma Ramona, Elizabeth Tuck, Anna Arutyunyan, Roser Vento-Tormo, Moritz Gerstung, Louisa James, Oliver Stegle, and Omer Ali Bayraktar. Cell2location maps fine-grained cell types in spatial transcriptomics. *Nature Biotechnology*, pages 1–11, 2022.

Shiquan Sun, Jiaqiang Zhu, and Xiang Zhou. Statistical analysis of spatial expression patterns for spatially resolved transcriptomic studies. *Nature Methods*, 17(2):193–200, 2020.

Valentine Svensson, Sarah A Teichmann, and Oliver Stegle. SpatialDE: identification of spatially variable genes. *Nature Methods*, 15(5):343–346, 2018.

Daniela F Quail and Johanna A Joyce. Microenvironmental regulation of tumor progression and metastasis. *Nature Medicine*, 19(11):1423–1437, 2013.

Isabella S. Kim, Silja Heilmann, Emily R. Kansler, Yan Zhang, Milena Zimmer, Kajan Ratnakumar, Robert L. Bowman, Theresa Simon-Vermot, Myles Fennell, Ralph Garippa, Liang Lu, William Lee, Travis Hollmann, Joao B. Xavier, and Richard M. White. Microenvironment-derived factors driving metastatic plasticity in melanoma. *Nature Communications*, 8(1):14343, 2017.

Hendrik Ungefroren, Susanne Sebens, Daniel Seidl, Hendrik Lehnert, and Ralf Hass. Interaction of tumor cells with the microenvironment. *Cell communication and signaling : CCS*, 9:18–18, 2011.

Sergei I Grivennikov, Florian R Greten, and Michael Karin. Immunity, inflammation, and cancer. *Cell*, 140(6):883–899, 2010.

Miranda V Hunter, Reuben Moncada, Joshua M Weiss, Itai Yanai, and Richard M White. Spatially resolved transcriptomics reveals the architecture of the tumor-microenvironment interface. *Nature communications*, 12(1):1–16, 2021.

Dylan M Cable, Evan Murray, Luli S Zou, Aleksandrina Goeva, Evan Z Macosko, Fei Chen, and Rafael A Irizarry. Robust decomposition of cell type mixtures in spatial transcriptomics. *Nature Biotechnology*, pages 1–10, 2021.

Kim Thrane, Hanna Eriksson, Jonas Maaskola, Johan Hansson, and Joakim Lundeberg. Spatially resolved transcriptomics enables dissection of genetic heterogeneity in stage iii cutaneous malignant melanoma. *Cancer Research*, 78(20):5970–5979, 2018.

Lawrence Hubert and Phipps Arabie. Comparing partitions. *Journal of Classification*, 2(1):193–218, 1985.

David M Blei, Andrew Y Ng, and Michael I Jordan. Latent Dirichlet allocation. *Journal of Machine Learning Research*, 3(Jan):993–1022, 2003.

Patrik L. Ståhl, Fredrik Salmén, Sanja Vickovic, Anna Lundmark, José Fernández Navarro, Jens Magnusson, Stefania Giacomello, Michaela Asp, Jakub O. Westholm, Mikael Huss, Annelie Mollbrink, Sten Linnarsson, Simone Codeluppi, Åke Borg, Fredrik Pontén, Paul Igor Costea, Pelin Sahlén, Jan Mulder, Olaf Bergmann, Joakim Lundeberg, and Jonas Frisén. Visualization and analysis of gene expression in tissue sections by spatial transcriptomics. *Science*, 353(6294):78–82, 2016. doi: 10.1126/science.aaf2403.

Sidharth V. Puram, Itay Tirosh, Anuraag S. Parikh, Anoop P. Patel, Keren Yizhak, Shawn Gillespie, Christopher Rodman, Christina L. Luo, Edmund A. Mroz, Kevin S. Emerick, Daniel G. Deschler, Mark A. Varvares, Ravi Mylvaganam, Orit Rozenblatt-Rosen, James W. Rocco, William C. Faquin, Derrick T. Lin, Aviv Regev, and Bradley E. Bernstein. Single-cell transcriptomic analysis of primary and metastatic tumor ecosystems in head and neck cancer. *Cell*, 171(7):1611–1624.e24, 2017. ISSN 0092-8674. doi: <https://doi.org/10.1016/j.cell.2017.10.044>.

Paola Marie Marcovecchio, Graham Thomas, and Shahram Salek-Ardakani. Cxcl9-expressing tumor-associated macrophages: new players in the fight against cancer. *Journal for Immunotherapy of Cancer*, 9(2), 2021.

Melvyn T Chow, Aleksandra J Ozga, Rachel L Servis, Dennie T Frederick, Jennifer A Lo, David E Fisher, Gordon J Freeman, Genevieve M Boland, and Andrew D Luster. Intratumoral activity of the cxcr3 chemokine system is required for the efficacy of anti-pd-1 therapy. *Immunity*, 50(6):1498–1512, 2019.

Anna Passarelli, Francesco Mannavola, Luigia Stefania Stucci, Marco Tucci, and Francesco Silvestris. Immune system and melanoma biology: a balance between immuno surveillance and immune escape. *Oncotarget*, 8(62):106132, 2017.

R Huber, B Meier, A Otsuka, G Fenini, T Satoh, S Gehrke, D Widmer, MP Levesque, J Mangana, K Kerl, C Gebhardt, H Fujii, C Nakashima, Y Nonomura, K Kabashima, R Dummer, E Contassot, and French LE. Tumour hypoxia promotes melanoma growth and metastasis via high mobility group box-1 and m2-like macrophages. *Scientific Reports*, 6(1):1–14, 2016.

James R. Faulkner and Vladimir N. Minin. Locally adaptive smoothing with Markov random fields and shrinkage priors. *Bayesian Analysis*, 13(1):225, 2018.

Wesley Tansey, Alex Athey, Alex Reinhart, and James G. Scott. Multiscale spatial density smoothing: An application to large-scale radiological survey and anomaly detection. *Journal of the American Statistical Association*, 112(519):1047–1063, 2017.

Anindya Bhadra, Jyotishka Datta, Nicholas G. Polson, and Brandon Willard. The horseshoe+ estimator of ultra-sparse signals. *Bayesian Analysis*, 12(4):1105–1131, 2017.

Bradley Efron. *Large-scale inference: Empirical Bayes methods for estimation, testing, and prediction*, volume 1. 2012.

Yosiyuki Sakamoto, Makio Ishiguro, and Genshiro Kitagawa. Akaike information criterion statistics. *Dordrecht, The Netherlands: D. Reidel*, 81(10.5555):26853, 1986.

Andrew A Neath and Joseph E Cavanaugh. The bayesian information criterion: background, derivation, and applications. *Wiley Interdisciplinary Reviews: Computational Statistics*, 4(2):199–203, 2012.